






Hundreds of weak lensing shear-selected clusters from the Hyper Suprime-Cam Subaru Strategic Program S19A data

Masamune OGURI,^{1,2,3,*} Satoshi MIYAZAKI,^{4,5} Xiangchong LI ,^{2,3}
Wentao LUO,³ Ikuyuki MITSUISHI,⁶ Hironao MIYATAKE,^{3,6,7} Surhud MORE,^{3,8}
Atsushi J. NISHIZAWA ,⁷ Nobuhiro OKABE ,^{9,10,11} Naomi OTA ,¹²
Andrés A. PLAZAS MALAGÓN,¹³ and Yousuke UTSUMI ¹⁴

¹Research Center for the Early Universe, The University of Tokyo, 7-3-1 Hongo, Bunkyo-ku, Tokyo 113-0033, Japan

²Department of Physics, The University of Tokyo, 7-3-1 Hongo, Bunkyo-ku, Tokyo 113-0033, Japan

³Kavli Institute for the Physics and Mathematics of the Universe (Kavli IPMU, WPI), The University of Tokyo, 5-1-5 Kashiwanoha, Kashiwa, Chiba 277-8583, Japan

⁴National Astronomical Observatory of Japan, 2-21-1 Osawa, Mitaka, Tokyo 181-8588, Japan

⁵SOKENDAI (The Graduate University for Advanced Studies), 2-21-1 Osawa, Mitaka, Tokyo 181-8588, Japan

⁶Division of Physics and Astrophysical Science, Graduate School of Science, Nagoya University, Nagoya, Aichi 464-8602, Japan

⁷Institute for Advanced Research, Nagoya University, Furo-cho, Chikusa-ku, Nagoya, Aichi 464-8602, Japan

⁸The Inter-University Center for Astronomy and Astrophysics (IUCAA), Post Bag 4, Ganeshkhind, Pune 411007, India

⁹Department of Physical Science, Hiroshima University, 1-3-1 Kagamiyama, Higashi-Hiroshima, Hiroshima 739-8526, Japan

¹⁰Hiroshima Astrophysical Science Center, Hiroshima University, 1-3-1 Kagamiyama, Higashi-Hiroshima, Hiroshima 739-8526, Japan

¹¹Core Research for Energetic Universe, Hiroshima University, 1-3-1 Kagamiyama, Higashi-Hiroshima, Hiroshima 739-8526, Japan

¹²Department of Physics, Nara Women's University, Kitauoyanishi-machi, Nara, Nara 630-8506, Japan

¹³Department of Astrophysical Sciences, Princeton University, Peyton Hall, Princeton, NJ 08544, USA

¹⁴Kavli Institute for Particle Astrophysics and Cosmology, SLAC National Accelerator Laboratory, Stanford University, Menlo Park, CA 94025, USA

*E-mail: masamune.oguri@ipmu.jp

Received 2021 March 29; Accepted 2021 April 30

Abstract

We use the Hyper Suprime-Cam Subaru Strategic Program S19A shape catalog to construct weak lensing shear-selected cluster samples. From aperture mass maps covering $\sim 510 \text{ deg}^2$ created using a truncated Gaussian filter, we construct a catalog of 187 shear-selected clusters that correspond to mass map peaks with signal-to-noise ratio larger

than 4.7. Most of the shear-selected clusters have counterparts in optically selected clusters, from which we estimate the purity of the catalog to be higher than 95%. The sample can be expanded to 418 shear-selected clusters with the same signal-to-noise ratio cut by optimizing the shape of the filter function and by combining weak lensing mass maps created with several different background galaxy selections. We argue that dilution and obscuration effects of cluster member galaxies can be mitigated by using background source galaxy samples and adopting a filter function with its inner boundary larger than about $2'$. The large samples of shear-selected clusters that are selected without relying on any baryonic tracer are useful for detailed studies of cluster astrophysics and cosmology.

Key words: dark matter — galaxies: clusters: general — gravitational lensing: weak — large-scale structure of universe

1 Introduction

Clusters of galaxies are the most massive gravitationally bound objects in the Universe and have proven to be a key class of objects for establishing the standard cosmological model that consists of dark matter and dark energy (for reviews, see, e.g., Allen et al. 2011; Kravtsov & Borgani 2012). We can study the internal structure and statistical properties of clusters of galaxies with multi-wavelength datasets, including optical, X-ray, and radio. For instance, a massive cluster of galaxies can be securely identified from an overdensity of cluster member galaxies with similar colors (e.g., Gladders & Yee 2000). X-rays from hot gas in clusters of galaxies provide an important means of finding and studying clusters of galaxies (e.g., Ebeling et al. 2001). Large samples of clusters are being constructed via the Sunyaev–Zel'dovich effect on cosmic microwave background fluctuations (e.g., Planck Collaboration 2016; Hilton et al. 2021).

The abundance and internal structure of clusters of galaxies are mainly determined by the dynamics of dark matter, which makes it critically important to study the distribution of dark matter in clusters in great detail. Weak gravitational lensing directly probes the dark matter distribution in clusters of galaxies and hence plays a key role in characterizing clusters (for a review see, e.g., Umetsu 2020). Among others, weak gravitational lensing plays an essential role in the use of the cluster population as a probe of cosmological parameters, because cluster observables must be linked to cluster masses in order to compare the observed abundance of clusters with theoretical predictions (for a review, see, e.g., Pratt et al. 2019). Indeed, attempts to use clusters as an accurate cosmological probe have often been hampered by the uncertainty of mass calibrations of clusters for which complicated selection biases in cluster surveys must be taken into account.

A new approach that has been explored less extensively is finding clusters directly from weak gravitational lensing shear data by identifying peaks in weak lensing mass maps (e.g., Schneider 1996; White et al. 2002; Hamana et al.

2004; Hennawi & Spergel 2005; Maturi et al. 2005, 2010; Fan et al. 2010; Marian et al. 2012; Lin et al. 2016). The abundance of the peaks contains information on the abundance of massive dark matter halos and hence on cosmological parameters (e.g., Jain & Van Waerbeke 2000; Dietrich & Hartlap 2010; Maturi et al. 2010; Shan et al. 2014; Liu et al. 2015a, 2015b; Hamana et al. 2015; Kacprzak et al. 2016; Shan et al. 2018). In addition, the relatively simple and clean selection function of weak lensing shear-selected clusters (e.g., Hamana et al. 2012; Chen et al. 2020) enables their use for better understanding of cluster astrophysics. For instance, X-ray analysis of shear-selected clusters suggests that they tend to be X-ray underluminous compared with clusters found in other techniques (Giles et al. 2015; Miyazaki et al. 2018b).

However, a challenge lies in the requirement of wide and deep imaging for finding a significant number of weak lensing shear-selected clusters. First attempts identified only a handful of such clusters, if restricted to those with a sufficiently high signal-to-noise ratio (see, e.g., the Appendix) of $\gtrsim 5$ (Wittman et al. 2001, 2006; Miyazaki et al. 2002, 2007; Hettterscheidt et al. 2005; Schirmer et al. 2007; Gavazzi & Soucail 2007; Utsumi et al. 2014). On the other hand, more systematic search of weak lensing shear-selected clusters is made possible thanks to recent progress in wide-field imaging surveys. For instance, Shan et al. (2012) constructed a sample of 51 shear-selected clusters with signal-to-noise ratios larger than 4.5 from the Canada-France-Hawaii Telescope Legacy Survey (Heymans et al. 2012).

Hyper Suprime-Cam (HSC; Miyazaki et al. 2018a), which is a wide-field optical imager mounted on the Subaru 8.2 m telescope, offers a unique opportunity for constructing a large sample of weak lensing shear-selected clusters (Miyazaki et al. 2015). In particular, the HSC Subaru Strategic Program (HSC-SSP; Aihara et al. 2018a, 2018b, 2019), which is a deep multi-band imaging survey of 1400 deg^2 of the sky, is an ideal survey for this purpose. Miyazaki et al. (2018b) presented a sample of 65 weak

lensing shear-selected clusters with signal-to-noise ratios larger than 4.7 from the HSC-SSP first-year shape catalog covering $\sim 160 \text{ deg}^2$ (Mandelbaum et al. 2018b). Using the same HSC S16A data, Hamana, Shirasaki, and Lin (2020) constructed a sample of 124 shear-selected clusters with signal-to-noise ratios larger than 5 by mitigating the dilution effect of foreground and cluster member galaxies.

In this paper, we present updated catalogs of weak lensing shear-selected clusters from the latest HSC-SSP S19A shape catalog covering $\sim 433 \text{ deg}^2$ (X. Li et al. in preparation). We construct catalogs using three different approaches adopting different shapes of filters. We also assign redshifts of individual clusters by cross-matching the shear-selected clusters with optically selected clusters.

This paper is organized as follows. The data used for our analysis are summarized in section 2. Our method for constructing mass maps is detailed in section 3. We present our main results in section 4, and conclude in section 5. Throughout the paper we assume the matter density $\Omega_m = 0.3$, the cosmological constant $\Omega_\Lambda = 0.7$, the baryon density $\Omega_b = 0.05$, the dimensionless Hubble constant $h = 0.7$, the spectral index $n_s = 0.96$, and the normalization of the matter power spectrum $\sigma_8 = 0.81$.

2 Data

2.1 Weak lensing shape catalog

The HSC-SSP S19A shape catalog (X. Li et al. in preparation) is constructed in a manner similar to the HSC-SSP S16A shape catalog presented in Mandelbaum et al. (2018b) that takes the moment-based approach of Hirata and Seljak (2003). The multiplicative and additive biases are derived with realistic image simulations (Mandelbaum et al. 2018a). The detailed systematics tests presented in X. Li et al. (in preparation) indicate that the S19A shape catalog is sufficiently accurate and is ready for various cosmological and astrophysical analyses. The catalog contains ~ 36 million galaxies.

Photometric redshifts of individual galaxies are also measured with various methods using the HSC *grizy*-band photometry (for photometric redshifts of galaxies in the S16A data, see Tanaka et al. 2018). In this paper we may use subsamples of the S19A shape catalog that are defined based on these photometric redshifts. Specifically, we define subsamples using the so-called P-cut method (see Oguri 2014; Medezinski et al. 2018), for which galaxies satisfying

$$\int_{z_{\min}}^{z_{\max}} P(z) dz > P_{\text{th}}, \quad (1)$$

where $P(z)$ is the probability distribution function (PDF) of the photometric redshift of each galaxy, are included.

This P-cut allows us to securely and flexibly select galaxies behind clusters of interest by choosing the parameters z_{\min} , z_{\max} , and P_{th} appropriately (see Medezinski et al. 2018), and hence mitigate the dilution effect by cluster member galaxies (see also Hamana et al. 2020). The performance of the P-cut method is shown to be comparable to the selection of background galaxies in color-color space (Medezinski et al. 2018).

Throughout the paper we adopt the dNNz photometric redshift measurement (A. J. Nishizawa et al. in preparation) for defining background galaxy samples with the P-cut method. This is based on the multiple-layer perceptron that consists of six hidden layers where each layer contains 100 nodes. Input attributes are `cmode1` magnitude, size, and point spread function matched aperture magnitude in five broad bands, leading to 15 attributes in total, for each galaxy. The outputs are probabilities of the galaxy lying at the redshift bin spanning from $z = 0$ to 7 divided into 100 bins. The code is trained to minimize the total difference between the output probabilities and input delta-function-like probability summed over all training sample and redshift ranges. From the analysis on the test sample that has not been used for training, it is found that redshifts are accurate with a bias of 10^{-4} , scatter of 3%, and outlier fraction of less than 10%. dNNz can avoid overfitting even when part of the data is missing (e.g., due to the lack of images in some broadband filters), by introducing a dropout layer right after an input layer with missing rate 0.2. When applying dNNz on real data, dNNz with the dropout layer is applied only when part of the data is missing, otherwise dNNz without the dropout layer is employed for the complete data to maximize the performance of the photometric redshift measurement.

2.2 Optically selected cluster catalogs

We use several optically selected cluster catalogs to assign redshifts for individual peaks in weak lensing mass maps. First, we adopt a cluster catalog (S20A version 1¹) constructed with the photometric data from the HSC-SSP S20A internal data release using the CAMIRA algorithm (Oguri 2014). In Oguri et al. (2018a), the CAMIRA algorithm was applied to the HSC-SSP S16A data covering $\sim 230 \text{ deg}^2$ to construct a catalog of 1921 clusters at redshift $0.1 < z < 1.1$ and richness N greater than 15 (for the definition of richness N in the CAMIRA algorithm, see Oguri 2014). In this paper, we adopt an updated catalog of 8910 clusters at

¹ While the S20A version 2 CAMIRA cluster catalog, which includes photometry corrections to mitigate various photometry issues (Aihara et al. 2019), is currently available, in this paper we use the version 1 catalog that was the latest version when the shear-selected cluster catalogs were constructed.

redshift $0.1 < z < 1.38$ and richness greater than 15 from the HSC-SSP S20A data covering $\sim 830 \text{ deg}^2$.

Since the HSC-SSP survey region is chosen to overlap with the Sloan Digital Sky Survey (SDSS; York et al. 2000), we also use SDSS cluster catalogs for assigning cluster redshifts. Specifically, we use the redMaPPer cluster catalog (Rykoff et al. 2014) that contains clusters at $0.08 < z < 0.6$ as well as the WHL15 cluster catalog (Wen et al. 2012; Wen & Han 2015) that contains clusters at $0.05 < z < 0.79$. Both of these cluster catalogs were constructed based on the photometric galaxy catalog covering $\sim 14000 \text{ deg}^2$ from SDSS Data Release 8 (DR8; Aihara et al. 2011). In addition to these purely optically selected clusters, we also adopt the CODEX cluster catalog (Finoguenov et al. 2020) that contains clusters at $0.05 < z < 0.69$ from the ROSAT all-sky survey (RASS; Voges et al. 1999) with optical confirmations using the redMaPPer algorithm applied to the SDSS DR8 data. Throughout the paper we use X-ray centroids as centers of the CODEX clusters.

All the cluster redshifts we adopt throughout this paper are photometric redshifts of clusters derived from the HSC *grizy*-band photometry for CAMIRA or from the SDSS *ugriz*-band photometry for redMaPPer, WHL15, and CODEX. The typical accuracy of these cluster photometric redshifts is $\sigma_z/(1+z) \sim 0.01$, which is sufficiently accurate for our current purpose.

3 Mass maps

3.1 Introduction

Since both convergence κ and shear γ are derived by the second derivatives of the lens potential, we can derive a convergence (mass) map from the shear map by convolution of the shear map with a kernel (Kaiser & Squires 1993). More generally, in the flat sky coordinate θ , we can construct a map of the aperture mass $M_{\text{ap}}(\theta)$ (Schneider 1996) which is a convergence convolved with a spatial filter U ,

$$M_{\text{ap}}(\theta) = \int d\theta' \kappa(\theta') U(|\theta - \theta'|). \quad (2)$$

Provided that the spatial filter is compensated,

$$\int d\theta \theta U(\theta) = 0, \quad (3)$$

this is equivalent to the convolution of the tangential shear with a kernel Q ,

$$M_{\text{ap}}(\theta) = \int d\theta' \gamma_+(\theta'; \theta) Q(|\theta - \theta'|), \quad (4)$$

where $\gamma_+(\theta'; \theta)$ is the tangential shear at θ' defined with respect to θ and Q is related to U as

$$Q(\theta) = \frac{2}{\theta^2} \int_0^\theta d\theta' \theta' U(\theta') - U(\theta). \quad (5)$$

In this paper, we consider two types of spatial filter. One is a truncated Gaussian filter, which resembles the one adopted by Miyazaki et al. (2018b) to construct a shear-selected cluster sample from the HSC S16A data (see also Hamana et al. 2020). The other is a filter introduced by Schneider (1996), which we call a truncated isothermal filter throughout the paper and is designed to optimize the detection of halos from mass maps. In the following subsections we describe these filters in more detail.

3.2 Truncated Gaussian filter

We use the following kernel function to define the truncated Gaussian filter,

$$Q(\theta) = \frac{1}{\pi\theta^2} \left[1 - \left(1 + \frac{\theta^2}{\theta_0^2} \right) e^{-\theta^2/\theta_0^2} \right] e^{-\theta^4/\theta_{\text{out}}^4}, \quad (6)$$

which is smoothly truncated at $\theta = \theta_{\text{out}}$. Thus, the filter is slightly different from the one adopted by Miyazaki et al. (2018b) and Hamana, Shirasaki, and Lin (2020), for which the kernel function is sharply truncated at $\theta = \theta_{\text{out}}$. We adopt this smoothly truncated form for the numerical stability of our approach to derive mass maps using the fast Fourier transform (see subsection 3.4). The corresponding spatial filter $U(\theta)$ can be derived as

$$U(\theta) = -Q(\theta) - \int_0^\theta d\theta' \frac{2}{\theta'} Q(\theta'). \quad (7)$$

Throughout the paper we adopt $\theta_0 = 1.5'$ and $\theta_{\text{out}} = 13'$, so that the resulting signal-to-noise ratios roughly match those in Miyazaki et al. (2018b) and Chen et al. (2020). Following Miyazaki et al. (2018b), we also do not apply any cut in the source galaxy sample. Hereafter, this set-up is referred to as TG15.

3.3 Truncated isothermal filter

Schneider (1996) introduced the following form of the spatial filter for the aperture mass:

$$U(\theta) = \begin{cases} 1 & (\theta \leq v_1\theta_R), \\ \frac{1}{1-c} \left[\frac{v_1\theta_R}{\sqrt{(\theta - v_1\theta_R)^2 + (v_1\theta_R)^2}} - c \right] & (v_1\theta_R \leq \theta \leq v_2\theta_R), \\ \frac{b}{\theta_R^3} (\theta_R - \theta)^2 (\theta - \alpha\theta_R) & (v_2\theta_R \leq \theta \leq \theta_R), \\ 0 & (\theta_R \leq \theta), \end{cases} \quad (8)$$

Table 1. Summary of set-ups to construct shear-selected cluster samples.

Name	Filter	Parameter values	Source galaxy selection	Num. galaxies
TG15	Truncated Gaussian	$\theta_0 = 1'.5, \theta_{\text{out}} = 13'$	No cut	35804886
TI05	Truncated isothermal	$\nu_1 = 0.021, \nu_2 = 0.36, \theta_R = 23'.8$	$z_{\text{min}} = 0.2, z_{\text{max}} = 7, P_{\text{th}} = 0.95$	32750421
	Truncated isothermal	$\nu_1 = 0.025, \nu_2 = 0.36, \theta_R = 20'.0$	$z_{\text{min}} = 0.3, z_{\text{max}} = 7, P_{\text{th}} = 0.95$	26024748
	Truncated isothermal	$\nu_1 = 0.027, \nu_2 = 0.36, \theta_R = 18'.5$	$z_{\text{min}} = 0.5, z_{\text{max}} = 7, P_{\text{th}} = 0.95$	20664165
	Truncated isothermal	$\nu_1 = 0.027, \nu_2 = 0.36, \theta_R = 18'.5$	$z_{\text{min}} = 0.7, z_{\text{max}} = 7, P_{\text{th}} = 0.95$	15564223
TI20	Truncated isothermal	$\nu_1 = 0.095, \nu_2 = 0.36, \theta_R = 21'.1$	$z_{\text{min}} = 0.2, z_{\text{max}} = 7, P_{\text{th}} = 0.95$	32750421
	Truncated isothermal	$\nu_1 = 0.110, \nu_2 = 0.36, \theta_R = 18'.2$	$z_{\text{min}} = 0.3, z_{\text{max}} = 7, P_{\text{th}} = 0.95$	26024748
	Truncated isothermal	$\nu_1 = 0.121, \nu_2 = 0.36, \theta_R = 16'.6$	$z_{\text{min}} = 0.5, z_{\text{max}} = 7, P_{\text{th}} = 0.95$	20664165
	Truncated isothermal	$\nu_1 = 0.121, \nu_2 = 0.36, \theta_R = 16'.6$	$z_{\text{min}} = 0.7, z_{\text{max}} = 7, P_{\text{th}} = 0.95$	15564223

where c, b, α are determined from the condition that $U(\theta)$ and its first derivative are continuous at $\theta = \nu_2 \theta_R$ as well as the compensation condition given by equation (3). This means that the shape of $U(\theta)$ is specified by three parameters, ν_1, ν_2 , and θ_R . The corresponding kernel function is derived using equation (5).

This filter has several desirable properties. First, we can tweak the shape of the filter quite flexibly by adjusting the three parameters ν_1, ν_2 , and θ_R . Second, it has $Q(\theta) = 0$ at $\theta < \nu_1 \theta_R$ and hence allows us to efficiently remove the contribution from the innermost part of halos, which is a source of various systematic effects on the signal such as the dilution effect by cluster member galaxies, the effect of reduced shear, and the magnification bias. Third, the filter is confined within a finite radius [i.e., $U(\theta) = Q(\theta) = 0$ at $\theta > \theta_R$] and hence mitigates the impact of, e.g., the boundary of the survey region on the map.

To explore the impact of the different inner boundary of the filter, $\nu_1 \theta_R$, in this paper we consider two different values of the inner boundary, $\nu_1 \theta_R = 0'.5$ and $2'$, which are referred as TI05 and TI20, respectively. For both TI05 and TI20, we construct mass maps with four different source galaxy subsamples defined using photometric redshifts of source galaxies (see subsection 2.1), in order to enhance the detection efficiency particularly at high redshifts (see also Hamana et al. 2020). For each inner boundary of the filter and source galaxy sample, we carefully choose parameter values of the filter to maximize the expected signal-to-noise ratio and to mitigate the impact of density fluctuations along the line of sight on cluster finding. The specific procedure for optimization of the parameters is detailed in the Appendix. Table 1 summarizes the set-ups for constructing shear-selected cluster samples. The shapes of the kernel function $Q(\theta)$ used in this paper are also presented in figure 1.

3.4 Practical procedure

Following Oguri et al. (2018b), we adopt the fast Fourier transform (FFT) to derive aperture mass maps from the

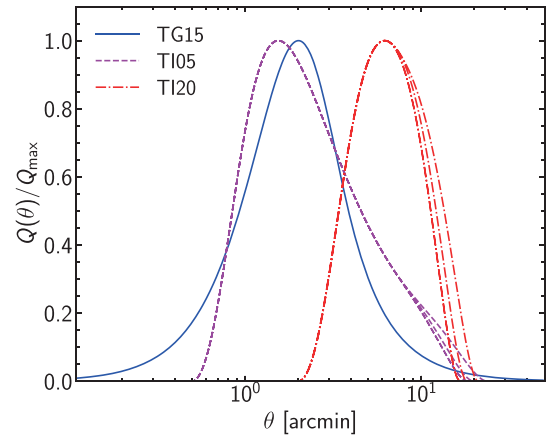


Fig. 1. The kernel function $Q(\theta)$, which is used to derive the aperture mass map [see equation (4)]. The solid, dashed, and dash-dotted lines are $Q(\theta)$ for the TG15, TI05, and TI20 set-ups summarized in table 1. Note that we adopt slightly different shapes of $Q(\theta)$ for different source galaxy selections. We show $Q(\theta)$ normalized by its maximum value. (Color online)

shape catalog. For a given source galaxy sample, we first create a shear map in a two-dimensional rectangular grid by a simple tangent plane projection. Throughout the paper, a grid pixel scale (θ -coordinate) of $\Delta\theta = 0'.25$ is adopted. We use a discrete version of equation (4) with weights to derive an aperture mass map, i.e.,

$$M_{\text{ap}}(\theta_i) = \frac{(\Delta\theta)^2}{W(\theta_i)} \sum_j w_j [\gamma_+(\theta_j; \theta_i) - c_{+,j}] Q(|\theta_i - \theta_j|), \quad (9)$$

$$W(\theta_i) = \frac{\sum_j w_j (1 + m_j) Q(|\theta_i - \theta_j|)}{\sum_j Q(|\theta_i - \theta_j|)}, \quad (10)$$

where i and j label each grid, w_i is the weight of the i th grid that is computed from the sum of weights of source galaxies in the grid, and $c_{+,i}$ and m_i denote the additive and multiplicative biases in the i th grid, respectively. We evaluate these summations by FFT with appropriate zero padding beyond the boundary. We also note that, due to the tangent

plane projection, the principal axes of the θ -coordinate are not necessarily aligned with the north and west directions, even for the HSC-SSP S19A patches (see below) whose areas are relatively small. Since the shear in the HSC-SSP shape catalog is defined with respect to the equatorial coordinate system, we rotate the shear so that the shear is converted to be defined with respect to the θ -coordinate. Furthermore, since the operation to create an aperture mass map [equation (9)] is confined within a relatively small sky area thanks to the compact size of the convolution kernel $Q(\theta)$, the flat-sky approximation is expected to be locally accurate in deriving each pixel value of the aperture mass map.

Since the HSC-SSP S19A shape catalog consists of six disjoint patches (XMM, VVDS, WIDE12H, GAMA09H, GAMA15H, and HECTOMAP), we create mass maps for each of these patches to search for peaks.

We define the signal-to-noise ratios of peaks using local estimates of the shape noise from the “sigma map” (Oguri et al. 2018b). We derive the sigma map by randomly rotating the orientations of source galaxies before constructing the mass map, and repeating this procedure 500 times. The sigma map is given by the square root of the variance of the randomized mass maps. The signal-to-noise ratio ν is defined by the ratio of the peak value of the mass map to the noise value at the peak position from the sigma map. We note that the sigma map derived by this procedure includes only the shape noise and hence does not include cosmic shear from the large-scale structure (see also the Appendix).

We mask the boundary of the survey region as follows. We first derive the smoothed number density map by first deriving the pixelized number density maps and then smoothing by a Gaussian kernel with a standard deviation of $8'$. The average number density is derived from the smoothed map with 3σ clipping. We mask pixels that have values less than 0.5 times the average number density. We also mask pixels with values of the sigma map more than 1.5 times higher than the average value.

From the map of the signal-to-noise ratio ν we select peaks with $\nu \geq 4.7$, which is the threshold also adopted by Miyazaki et al. (2018b). To avoid double counting of clusters, we discard any peaks that have other peaks with higher ν within $4'$. For mass maps with the truncated isothermal filter (TI05 and TI20), we create mass maps with four different values of z_{\min} as shown in table 1. We create a list of peaks for each value of z_{\min} , and combine the four lists of peaks with a matching radius of $4'$. For a peak that is detected in multiple mass maps from different source galaxy selections, we adopt the highest value of ν among the mass maps as the signal-to-noise ratio of that peak.

4 Results

4.1 Shear-selected cluster catalogs and redshift assignments

We construct shear-selected cluster catalogs from peaks with $\nu \geq 4.7$ in mass maps covering $\sim 510 \text{ deg}^2$ following the procedure described in subsection 3.4. The catalogs are constructed for the three set-ups (TG15, TI05, and TI20) summarized in table 1. The catalogs contain 187, 418, and 200 clusters for TG15, TI05, and TI20, respectively. Compared with the TG15 set-up adopted in Miyazaki et al. (2018b), we find roughly twice the number of shear-selected clusters for TI05, because the shape of the kernel function for TI05 follows the expected tangential shear profile more closely than for TG15 and therefore is more optimal. The small number of shear-selected clusters for TI20, on the other hand, is due to the removal of the large central region ($< 2'$) where a significant tangential shear signal is observed for many clusters. Figure 2 shows the spatial distribution of these clusters from peaks in mass maps. We note that, even though the numbers of shear-selected clusters are similar between TG15 and TI20, roughly half of the clusters are detected both in TG15 and TI20, partly because most of the clusters have signal-to-noise ratios near the threshold (see below).

To check whether they are indeed associated with concentrations of red galaxies, and to assign redshifts to these clusters, we cross match the shear-selected cluster catalogs with four optically selected cluster catalogs, HSC CAMIRA, SDSS redMaPPer, SDSS WHL15, and SDSS CODEX (see subsection 2.2 for concise descriptions of these catalogs). We regard any optically selected clusters that are located within the physical transverse distance of $1h^{-1} \text{ Mpc}$ computed at the cluster redshifts from each shear-selected cluster as matched clusters. It is possible that multiple optically selected clusters are matched with a single shear-selected cluster, and in that case we regard as a primary match the optically selected cluster that is located closest, in terms of the physical transverse distance, to the shear-selected cluster, whose location refers to a peak position in a mass map; we assign the photometric redshift of the primary matched cluster to the shear-selected cluster.

The result of this matching is summarized in table 2. For TG15 and TI20, $\sim 97\%$ of shear-selected clusters have counterparts in optically selected cluster catalogs and hence have redshift assignments. The fraction slightly decreases to $\sim 94\%$ for TI05. For comparison, we generate a random catalog of shear-selected clusters by randomly drawing points in unmasked regions of mass maps with a number density of 5 deg^{-2} , and apply the same method for matching shear-selected clusters with optically selected clusters to find that $\sim 33\%$ of the random shear-selected clusters are

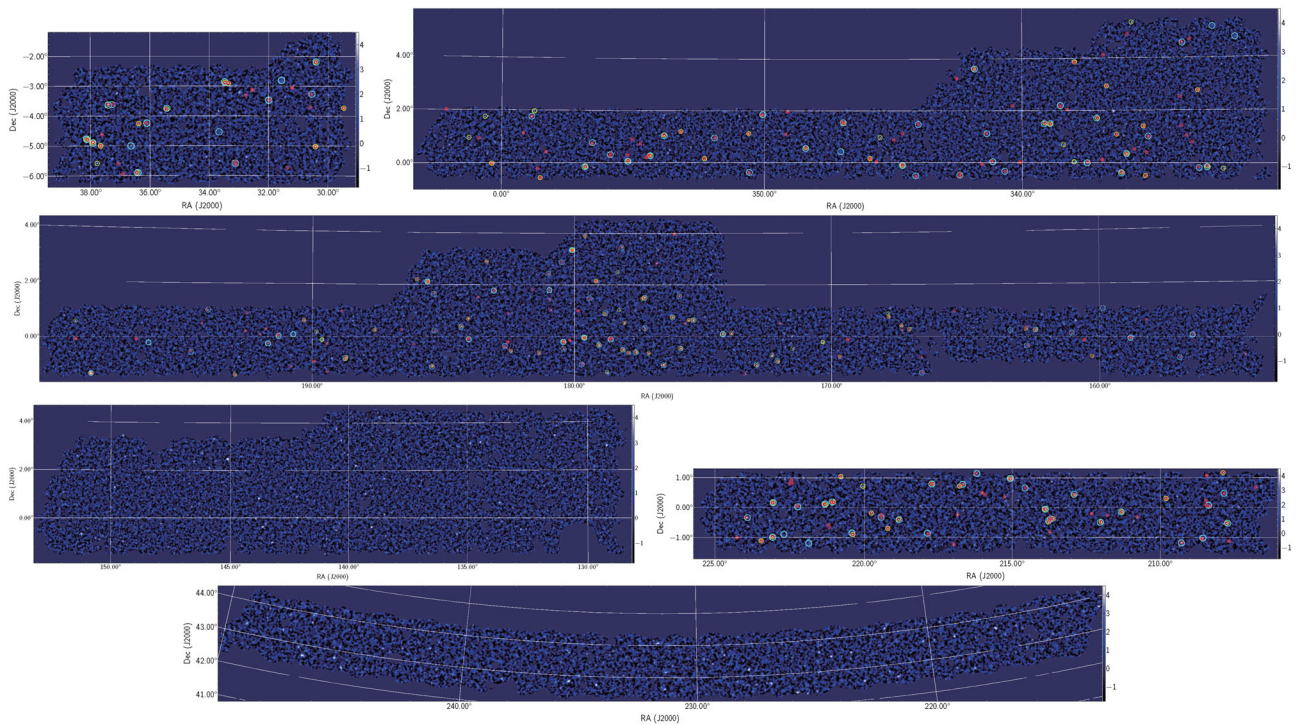


Fig. 2. Spatial distribution of identified shear-selected clusters, i.e., peaks in mass maps, in six disjoint patches. The middle-sized green, small red, and large cyan circles show clusters by TG15, TI05, and TI20 set-ups (see table 1), respectively. They are overlaid in mass maps created by the Gaussian filter without truncation [$\theta_{\text{out}} \rightarrow \infty$ in equation (6)] with $\theta_0 = 2'$. (Color online)

Table 2. Summary of shear-selected cluster samples and matching with optically selected cluster catalogs.*

Name	Num. clusters	CAMIRA match [†]	redMaPPer match [†]	WHL15 match [†]	CODEX match [†]	Any match
TG15	187	163 (21)	135 (7)	177 (50)	59 (6)	182
TI05	418	353 (51)	271 (11)	364 (104)	124 (6)	392
TI20	200	173 (33)	138 (10)	184 (69)	79 (3)	193

*The last column shows the number of shear-selected clusters that are matched with any of the optically selected cluster catalogs and thus with redshift assignments.

[†]The number in parentheses indicates shear-selected clusters that are matched with multiple optically selected clusters.

matched with optically selected clusters. Since this fraction represents the chance probability of matching with an optically selected cluster, we can argue that the true fraction of unmatched shear-selected clusters may be as high as $3 \times 3/2 \sim 5\%$ for TG15 and TI20, and $6 \times 3/2 \sim 9\%$ for TI05. Taking the incompleteness of our optically selected cluster samples used for matching (e.g., no cluster at $z < 0.05$) into consideration, we can argue that the purity of our shear-selected cluster catalogs is higher than 95% for TG15 and TI20, and more than 91% for TI05. The catalogs of the shear-selected clusters for the TG15, TI05, and TI20 set-ups including the results of cross matching are shown in supplementary tables 1, 2, and 3, available in the online version of this article.

We show the distributions of the signal-to-noise ratio ν and the redshift z_{cl} of shear-selected clusters for all three set-ups in figures 3 and 4, respectively. Number counts rapidly

decrease with increasing ν , and the redshift distributions peak at $z_{\text{cl}} \sim 0.2\text{--}0.3$, both of which are consistent with theoretical predictions (see, e.g., Miyazaki et al. 2018b).

While weak lensing mass maps are constructed from E-mode shear, B-mode mass maps generated from B-mode shear provide an important means of checking the validity of the analysis (e.g., Utsumi et al. 2014). As a sanity check, we select mass map peaks from B-mode mass maps adopting the same signal-to-noise ratio threshold of $\nu \geq 4.7$. The distribution of B-mode mass map peaks is also shown in figure 3. In total there are 6, 17, and 3 B-mode mass map peaks with $\nu \geq 4.7$ for TG15, TI05, and TI20, respectively. We find that the numbers of B-mode mass map peaks are sufficiently small, $\lesssim 4\%$, compared with those of E-mode mass map peaks, which supports the high purity of our shear-selected cluster catalogs as estimated above.

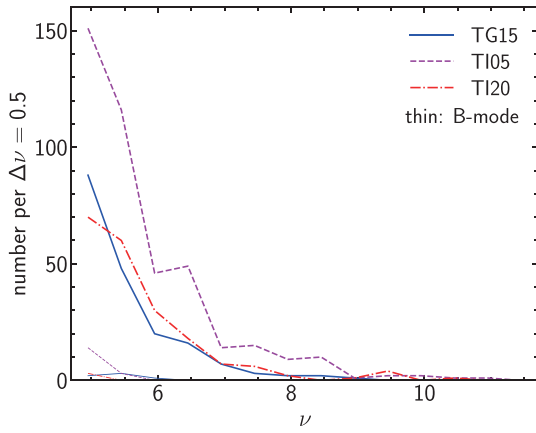


Fig. 3. Distributions of the signal-to-noise ratio ν . The solid, dashed, and dash-dotted lines show the distributions for the TG15, TI05, TI20 set-ups summarized in table 1, respectively. The thin lines indicate the distributions of the signal-to-noise ratio ν from B-mode mass map peaks. (Color online)

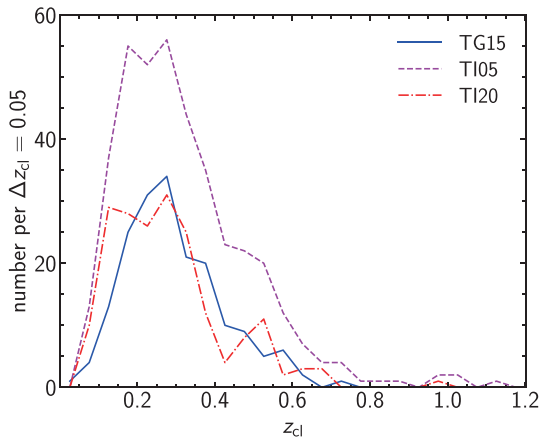


Fig. 4. Similar to figure 3, but showing distributions of cluster redshift z_{cl} . (Color online)

In figure 5, we show distributions of the physical transverse distance between the shear-selected cluster and the primary matched optically selected cluster. We find that in most cases the distance is small, $\lesssim 0.3 h^{-1} \text{Mpc}$. The mean distance is higher for TI20 than in the other set-ups, which can be understood by the conservative choice of $Q(\theta)$ to remove the small-scale information (see figure 1), which naturally leads to the degraded angular resolution of the resulting mass maps. For comparison, we also plot the distribution when using the random catalog mentioned above. Since the spatial distribution of the random catalog is not correlated with any optically selected clusters, the resulting distribution indicates that expected for matching by chance. We find that the distribution for the random catalog differs considerably from those for shear-selected clusters, supporting the high purity of our shear-selected cluster catalogs.

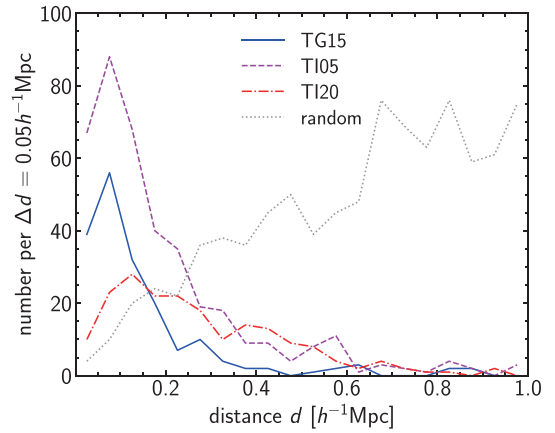


Fig. 5. Similar to figure 3, but showing distributions of the physical transverse distance d between the shear-selected cluster and the primary matched optically selected cluster. The distribution of d for the case using the random catalog is also shown by the dotted line for reference. (Color online)

4.2 Weak lensing mass measurements

Following Miyazaki et al. (2018b), we derive the weak lensing masses of all the shear-selected clusters with redshift assignments by fitting their differential surface density profiles. We use the P-cut method (Oguri 2014; Medezinski et al. 2018) to securely select background galaxies for each shear-selected cluster, adopting $z_{\min} = z_{cl} + 0.2$ and $P_{th} = 0.98$ in equation (1). We derive the differential surface density profile $\Delta\Sigma(R)$ by fully taking account of the PDF of the photometric redshift of each galaxy (for a specific procedure, see, e.g., Medezinski et al. 2018), again adopting the dNNz photometric redshift measurements. For TG15, we derive differential surface density profiles in the range $R = [0.3, 7] h^{-1} \text{Mpc}$ with a spacing of $\Delta\log R = 0.09$. The outer radius is chosen to be same as that used in Miyazaki et al. (2018b) and Chen et al. (2020), so that the mass bias derived in Chen et al. (2020) can be applied. We adopt a slightly larger inner boundary of $R = 0.3 h^{-1} \text{Mpc}$ to mitigate the dilution effect by cluster member galaxies (Medezinski et al. 2018). For TI05 and TI20, we adopt a more conservative radius range of $R = [0.3, 3] h^{-1} \text{Mpc}$. In all cases, we consider the shape noise and ignore the cosmic shear error, again to follow the set-up assumed in Chen et al. (2020).

The differential surface density profiles are fitted with a Navarro–Frenk–White (NFW) profile (Navarro et al. 1997), which describes differential surface density profiles of clusters in numerical simulations reasonably well out to ~ 10 times the virial radius (Oguri & Hamana 2011). We parameterize the NFW profile by M_{500c} and c_{500c} , which describe the mass and concentration parameter for the critical overdensity of 500. We restrict the range of the concentration parameter to $0.5 < c_{500c} < 10$ and derive both M_{500c} and c_{500c} from fitting to the observed differential surface

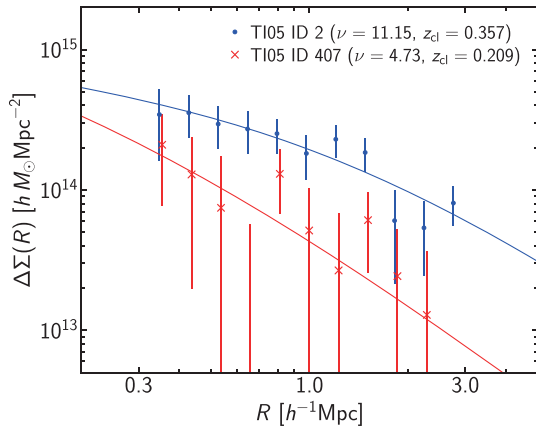


Fig. 6. Examples of tangential shear profiles and fitting them with an NFW profile. We show examples for high and low signal-to-noise ratio ν from the TI05 catalog. Symbols with errors show the observed tangential shear profiles, and lines indicate best-fitting NFW profiles. The errors include only the shape noise. (Color online)

density profile of each cluster. We show some examples of our tangential shear profile fitting in figure 6.

The derived weak lensing masses for the TG15, TI05, and TI20 catalogs as a function of the cluster redshift are shown in figure 7. The fitting results are also given in supplementary tables 1, 2, and 3. The increasing trend of weak lensing masses with increasing cluster redshift is theoretically expected for shear-selected clusters (see, e.g., Miyazaki et al. 2018b). The massive ($M_{500c} \sim 10^{15} h^{-1} M_{\odot}$) cluster at $z_{cl} \sim 0.18$ is the well-known cluster Abell 1689 that has one of the largest Einstein radii known (e.g., Oguri & Blandford 2009). Our weak lensing mass estimation of Abell 1689 is consistent with more careful lensing mass estimates in the literature (e.g., Umetsu & Broadhurst 2008; Umetsu et al. 2015).

In figure 7, we indicate clusters that are matched with the CODEX catalog. Only less than half of shear-selected clusters are matched with CODEX clusters (see also table 1), which is partly due to the shallow RASS X-ray data that is used to construct the CODEX catalog (Finoguenov et al.

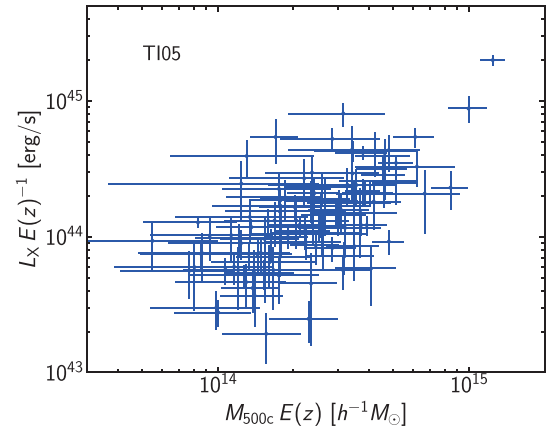


Fig. 8. Weak lensing masses of shear-selected clusters in the TI05 catalog compared with X-ray luminosities of CODEX clusters that are matched with the shear-selected clusters, with the correction of the dimensionless Hubble parameter $E(z)$. The X-ray luminosities are measured in the rest-frame 0.1–2.4 keV (Finoguenov et al. 2020). (Color online)

2020). As a sanity check, we compare our weak lensing masses with X-ray luminosities provided by the CODEX catalog. Figure 8 shows the comparison of weak lensing masses with X-ray luminosities for the TI05 catalog. As expected, we find a good correlation between the masses and the X-ray luminosities. We note that deriving the underlying scaling relation requires the correction of selection biases of both the weak lensing selections in HSC-SSP and the X-ray selection in RASS. We plan to study the X-ray properties of these shear-selected clusters in more detail using the eROSITA Final Equatorial Depth Survey data that are much deeper than the RASS X-ray data, which will be reported in a separate paper (M. Ramos-Ceja et al. in preparation).

4.3 Effects of cluster member galaxies

Cluster member galaxies affect weak lensing measurements in two main ways. One is the enhancement of the number

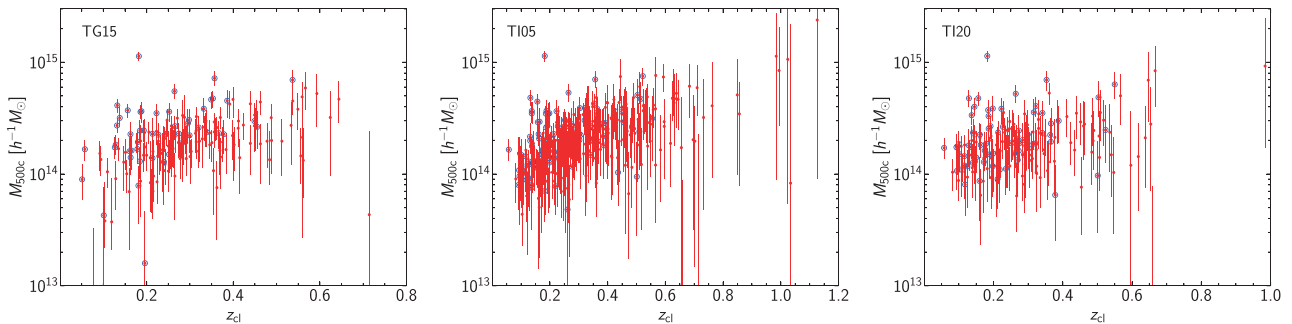


Fig. 7. Weak lensing masses and redshifts of shear-selected clusters in the TG15 (left), TI05 (middle), and TI20 (right) catalogs. The red filled circles with 1σ error bars show M_{500c} derived from differential surface density profile fitting. The blue open circles indicate clusters that are matched with the CODEX catalog. (Color online)

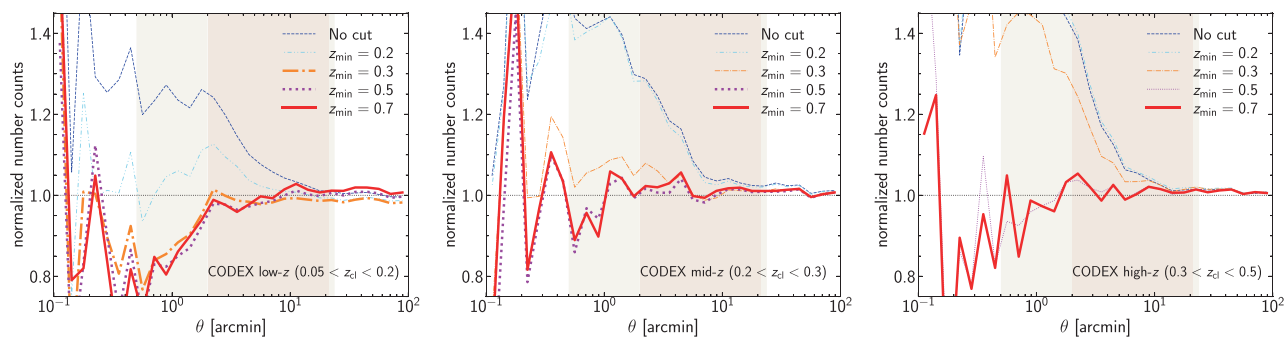


Fig. 9. Stacked number density profiles of source galaxies around CODEX clusters. Here we show number density profiles relative to those from random source catalogs with their total numbers matched to the total numbers of source galaxy samples such that the normalized number density profile should be unity if there is no effect of cluster member galaxies. The different lines show the results for the different source galaxy samples summarized in table 1. From left to right, stacking is conducted around low-redshift clusters at $0.05 < z_{cl} < 0.2$ with richness $\lambda > 25$, intermediate redshift clusters at $0.2 < z_{cl} < 0.3$ with $\lambda > 30$, and high-redshift clusters at $0.3 < z_{cl} < 0.4$ with $\lambda > 40$. The results for background source galaxy samples satisfying $z_{min} \geq z_{cl} + 0.1$ for all the clusters are highlighted by thick lines. The narrow and wide shaded regions indicate the non-zero ranges of the kernel function $Q(\theta)$ for TI20 and TI05, respectively (see also figure 1). (Color online)

density of source galaxies due to the contribution of cluster member galaxies, which dilutes weak lensing signals. The other is the diminishment of the number density of source galaxies due to the obscuration of small galaxies by cluster member galaxies. The former effect can be mitigated by using only source galaxies located behind clusters for weak lensing measurements. Since these effects are more pronounced near centers of clusters, choosing the kernel function $Q(\theta)$ that has a smaller contribution from small θ can also mitigate the effects of cluster member galaxies. Here we check the number density profiles of our source galaxy samples around massive clusters to check how our weak lensing mass maps are affected by cluster member galaxies.

To reduce the statistical noise, we derive stacked number density profiles of source galaxies for samples of massive clusters. Purely optically selected clusters are not ideal for this purpose, because some optically selected clusters exhibit large off-centering up to ~ 1 Mpc, which needs to be taken into account when interpreting observed stacked number density profiles. Thus, we adopt the CODEX cluster catalog and stack number density profiles around the X-ray centroids of CODEX clusters, because X-ray emission peaks are expected to be close to halo centers (e.g., Zhang et al. 2019).

Figure 9 shows stacked number density profiles for three CODEX cluster samples with different cluster redshifts. We also apply the richness cut for each cluster sample in order to select clusters with many cluster member galaxies, where the richness λ for CODEX clusters is measured using the redMaPPer algorithm (Rykoff et al. 2014). The richness threshold is determined so that a sufficient ($\gtrsim 50$) number of clusters is included in each of the cluster subsamples. We show stacked number density profiles normalized by those computed with random source galaxy catalogs in

order to highlight the effects of cluster member galaxies. We find a clear signature of the enhancement of number density profiles without any background galaxy selection. On the other hand, when source galaxies behind clusters are selected, we see decrements toward cluster centers due to the obscuration by cluster member galaxies (or magnification effects, see, e.g., Chiu et al. 2020). We find that the decrements are negligibly small at $\theta > 2'$, suggesting that the TI20 catalog is little affected by cluster member galaxy obscurations. In contrast, the TG15 and TI05 catalogs are more or less affected by cluster member galaxies in the sense that the observed signal-to-noise ratios may be affected by the dilution or obscuration effect due to cluster member galaxies. Since cluster member galaxies do not contribute to the signal, the dilution effect enhances the noise and reduces the signal-to-noise ratio. The obscuration affects both the signal and the noise in a complicated manner. These effects may need to be taken into account when deriving an accurate selection function for shear-selected clusters in the TG15 and TI05 catalogs.

5 Conclusion

We have constructed shear-selected cluster catalogs by selecting peaks in weak lensing aperture mass maps covering $\sim 510 \text{ deg}^2$ reconstructed by the HSC-SSP S19A shape catalog. Aperture mass maps are constructed using the truncated Gaussian filter (TG15) as well as the truncated isothermal filter with an inner boundary of $0.5'$ (TI05) and $2'$ (TI20). For TI05 and TI20, we employ multiple source galaxy subsamples for which galaxies below redshift z_{min} are removed to improve the efficiency. With a signal-to-noise ratio threshold of 4.7, our shear-selected cluster catalogs contain 187, 418, and 200 clusters for the TG15, TI05,

and TI20 set-ups, respectively. Cross matching with optically selected cluster catalogs suggests that the purity of the catalogs is high, more than 95% for TG15 and TI20 and more than 91% for TI05.

These catalogs represent by far the largest catalogs of shear-selected clusters to date with such a high signal-to-noise threshold, and will be useful for detailed studies of cluster astrophysics and cosmology. In this paper, we have demonstrated how the shape of the kernel function for constructing the aperture mass map can be optimized by adopting a flexible functional form of the filter function proposed by Schneider (1996). In particular, we have found that it is possible to choose the filter function such that it is almost free from effects of cluster member galaxies yet can select a sufficiently large number of clusters. Such a clean shear-selected cluster sample will be useful for obtaining accurate and robust constraints on cosmological parameters from the cluster abundance, in contrast to optically selected clusters for which constraining power appears to be limited by various systematic effects (Abbott et al. 2020). We will explore cosmological constraints with shear-selected clusters in a forthcoming paper.

Supplementary data

Supplementary tables 1, 2, and 3 are available online.

Acknowledgement

We thank T. Hamana and K. Umetsu for useful discussions and comments. This work was supported in part by the World Premier International Research Center Initiative (WPI Initiative), MEXT, Japan, and JSPS KAKENHI Grant Nos. JP18K03693, JP20H00181, JP20H05856. This work was supported in part by Japan Science and Technology Agency (JST) CREST JPMHCR1414, and by JST AIP Acceleration Research Grant No. JP20317829, Japan.

The Hyper Suprime-Cam (HSC) collaboration includes the astronomical communities of Japan and Taiwan, and Princeton University. The HSC instrumentation and software were developed by the National Astronomical Observatory of Japan (NAOJ), the Kavli Institute for the Physics and Mathematics of the Universe (Kavli IPMU), the University of Tokyo, the High Energy Accelerator Research Organization (KEK), the Academia Sinica Institute for Astronomy and Astrophysics in Taiwan (ASIAA), and Princeton University. Funding was contributed by the FIRST program from the Japanese Cabinet Office, the Ministry of Education, Culture, Sports, Science and Technology (MEXT), the Japan Society for the Promotion of Science (JSPS), the Japan Science and Technology Agency (JST), the Toray Science Foundation, NAOJ, Kavli IPMU, KEK, ASIAA, and Princeton University.

This paper makes use of software developed for the Large Synoptic Survey Telescope. We thank the LSST Project for making their code available as free software at <http://dm.lsst.org>.

This paper is based on data collected at the Subaru Telescope and retrieved from the HSC data archive system, which is operated by the Subaru Telescope and Astronomy Data Center (ADC) at NAOJ.

Data analysis was in part carried out with the cooperation of the Center for Computational Astrophysics (CfCA), NAOJ.

The Pan-STARRS1 Surveys (PS1) and the PS1 public science archive have been made possible through contributions by the Institute for Astronomy, the University of Hawaii, the Pan-STARRS Project Office, the Max Planck Society and its participating institutes, the Max Planck Institute for Astronomy, Heidelberg, and the Max Planck Institute for Extraterrestrial Physics, Garching, The Johns Hopkins University, Durham University, the University of Edinburgh, the Queen's University Belfast, the Harvard-Smithsonian Center for Astrophysics, the Las Cumbres Observatory Global Telescope Network Incorporated, the National Central University of Taiwan, the Space Telescope Science Institute, the National Aeronautics and Space Administration under grant no. NNX08AR22G issued through the Planetary Science Division of the NASA Science Mission Directorate, the National Science Foundation grant no. AST-1238877, the University of Maryland, Eotvos Lorand University (ELTE), the Los Alamos National Laboratory, and the Gordon and Betty Moore Foundation.

Appendix. Optimization of the truncated isothermal filter

We use signal-to-noise ratios of mass map peaks computed assuming the NFW profile (Navarro et al. 1997) to optimize parameters of the truncated isothermal filter presented in subsection 3.3. For each set of parameters, we compute the aperture mass $M_{\text{ap,NFW}}$ at the center of a halo using equation (2) with the convergence assuming an NFW profile (e.g., Bartelmann 1996). For each subsample of source galaxies given in table 1, we fully take account of the source redshift distribution by adopting the stacked PDF of the photometric redshift PDFs of all the source galaxies. We also adopt the fitting form of the mass-concentration relation presented by Diemer and Kravtsov (2015) and Diemer and Joyce (2019). The signal-to-noise ratio is then computed as

$$\nu_{\text{NFW}} = \frac{M_{\text{ap,NFW}}}{\sigma_{\text{shape}}}, \quad (\text{A1})$$

where σ_{shape} describes the shape noise of the filtered convergence field, computed as

$$\sigma_{\text{shape}} = \sigma_e \sqrt{\frac{\pi \int d\theta \theta Q^2(\theta)}{n_{\text{gal}}}}, \quad (\text{A2})$$

with σ_e and n_{gal} being the root-mean-square of the ellipticity and the number density of source galaxies, respectively. In this calculation we simply assume $\sigma_e = 0.4$ and $n_{\text{gal}} = 22 \text{ arcmin}^{-2}$ before any source galaxy selection so that the resulting noise of the mass map roughly coincides with that from the real data. For each source galaxy selection we reduce n_{gal} according to the weighted sum of the number of galaxies after the source galaxy selection.

While it is customary to define a sample of shear-selected clusters by applying a threshold to the signal-to-noise ratio that is defined in a manner similar to equation (A1) where only the shape noise is considered, it is known that the accumulated density fluctuations along the line of sight (i.e., cosmic shear) also contribute to the noise:

$$\sigma_{\text{LSS}} = \sqrt{\int \frac{\ell d\ell}{2\pi} |\hat{U}(\ell)|^2 C_\ell}, \quad (\text{A3})$$

where $\hat{U}(\ell)$ is the Fourier counterpart of the filter $U(\theta)$ and the cosmic shear power spectrum C_ℓ is related to the nonlinear matter power spectrum $P_m(k; z)$ as

$$C_\ell = \int d\chi \frac{[W^\kappa(\chi)]^2}{\chi^2} P_m(k = \ell/\chi; z), \quad (\text{A4})$$

$$W^\kappa(\chi) = \int_z^\infty dz_s \frac{4\pi G}{c^2} \frac{(\chi_s - \chi)\chi}{\chi_s(1+z)^2} \bar{\rho}_m p(z_s), \quad (\text{A5})$$

where χ and χ_s are the comoving radial distances corresponding to redshifts z and z_s , respectively, and $p(z_s)$ denotes the redshift distribution of the source galaxies. We use the revised `halofit` model of Takahashi et al. (2012) to compute $P_m(k; z)$. The signal-to-noise ratio including the large-scale structure noise is simply calculated as

$$\nu_{\text{NFW, wLSS}} = \frac{M_{\text{ap, NFW}}}{\sqrt{\sigma_{\text{shape}}^2 + \sigma_{\text{LSS}}^2}}. \quad (\text{A6})$$

We optimize the parameters of the truncated isothermal filter as follows. For each source galaxy selection listed in table 1, we consider NFW halos located at $z = z_{\text{min}} - 0.1$ with varying halo mass as representative halos detected in mass maps with the source galaxy selection characterized by z_{min} . For each mass of the NFW halo, we vary ν_1 , ν_2 , and θ_R to search for the optimal set of parameters that maximizes $\nu_{\text{NFW, wLSS}}$ given by equation (A6). Since the combination of $\nu_1\theta_R$ determines the inner boundary of the filter (see subsection 3.3), in this paper we consider two cases, $\nu_1\theta_R = 0.5$ and $2'$. The former is chosen to include the tangential shear at $\theta \sim 1' - 1.5'$, where the contribution to the signal is large. The latter removes a significant fraction of the inner part of the profile from the calculation, and hence is much less affected by various systematic effects as discussed in subsection 3.3 (see also subsection 4.3). First, we vary all three parameters with the constraint on $\nu_1\theta_R$ to find that $\nu_{\text{NFW, wLSS}}$ is generally maximized for $\nu_2 \sim 0.3-0.4$. We thus fix $\nu_2 = 0.36$ throughout the paper and derive the optimal choice of ν_1 and θ_R , as well as ν_{NFW} and $\nu_{\text{NFW, wLSS}}$, as a function of the halo mass. We adopt values of ν_1 and θ_R for the halo mass that yield $\nu_{\text{NFW}} \sim 5$, roughly corresponding

to the threshold of constructing shear-selected clusters used in the literature. Parameters determined by this procedure for each $\nu_1\theta_R$ and the source galaxy selection are presented in table 1.

References

- Abbott, T. M. C., et al. 2020, *Phys. Rev. D*, 102, 023509
Aihara, H., et al. 2011, *ApJS*, 193, 29
Aihara, H., et al. 2018a, *PASJ*, 70, S4
Aihara, H., et al. 2018b, *PASJ*, 70, S8
Aihara, H., et al. 2019, *PASJ*, 71, 114
Allen, S. W., Evrard, A. E., & Mantz, A. B. 2011, *ARA&A*, 49, 409
Bartelmann, M. 1996, *A&A*, 313, 697
Chen, K.-F., Oguri, M., Lin, Y.-T., & Miyazaki, S. 2020, *ApJ*, 891, 139
Chiu, I. N., Umetsu, K., Murata, R., Medezinski, E., & Oguri, M. 2020, *MNRAS*, 495, 428
Diemer, B., & Joyce, M. 2019, *ApJ*, 871, 168
Diemer, B., & Kravtsov, A. V. 2015, *ApJ*, 799, 108
Dietrich, J. P., & Hartlap, J. 2010, *MNRAS*, 402, 1049
Ebeling, H., Edge, A. C., & Henry, J. P. 2001, *ApJ*, 553, 668
Fan, Z., Shan, H., & Liu, J. 2010, *ApJ*, 719, 1408
Finoguenov, A., et al. 2020, *A&A*, 638, A114
Gavazzi, R., & Soucail, G. 2007, *A&A*, 462, 459
Giles, P. A., Maughan, B. J., Hamana, T., Miyazaki, S., Birkinshaw, M., Ellis, R. S., & Massey, R. 2015, *MNRAS*, 447, 3044
Gladders, M. D., & Yee, H. K. C. 2000, *AJ*, 120, 2148
Hamana, T., Oguri, M., Shirasaki, M., & Sato, M. 2012, *MNRAS*, 425, 2287
Hamana, T., Sakurai, J., Koike, M., & Miller, L. 2015, *PASJ*, 67, 34
Hamana, T., Shirasaki, M., & Lin, Y.-T. 2020, *PASJ*, 72, 78
Hamana, T., Takada, M., & Yoshida, N. 2004, *MNRAS*, 350, 893
Hennawi, J. F., & Spergel, D. N. 2005, *ApJ*, 624, 59
Hettterscheidt, M., Erben, T., Schneider, P., Maoli, R., van Waerbeke, L., & Mellier, Y. 2005, *A&A*, 442, 43
Heymans, C., et al. 2012, *MNRAS*, 427, 146
Hilton, M., et al. 2021, *ApJS*, 253, 3
Hirata, C., & Seljak, U. 2003, *MNRAS*, 343, 459
Jain, B., & Van Waerbeke, L. 2000, *ApJ*, 530, L1
Kacprzak, T., et al. 2016, *MNRAS*, 463, 3653
Kaiser, N., & Squires, G. 1993, *ApJ*, 404, 441
Kravtsov, A. V., & Borgani, S. 2012, *ARA&A*, 50, 353
Lin, C.-A., Kilbinger, M., & Pires, S. 2016, *A&A*, 593, A88
Liu, X., et al. 2015a, *MNRAS*, 450, 2888
Liu, J., Petri, A., Haiman, Z., Hui, L., Kratochvil, J. M., & May, M. 2015b, *Phys. Rev. D*, 91, 063507
Mandelbaum, R., et al. 2018a, *MNRAS*, 481, 3170
Mandelbaum, R., et al. 2018b, *PASJ*, 70, S25
Marian, L., Smith, R. E., Hilbert, S., & Schneider, P. 2012, *MNRAS*, 423, 1711
Maturi, M., Angrick, C., Pace, F., & Bartelmann, M. 2010, *A&A*, 519, A23
Maturi, M., Meneghetti, M., Bartelmann, M., Dolag, K., & Moscardini, L. 2005, *A&A*, 442, 851
Medezinski, E., et al. 2018, *PASJ*, 70, 30
Miyazaki, S., et al. 2002, *ApJ*, 580, L97

- Miyazaki, S., et al. 2015, *ApJ*, 807, 22
Miyazaki, S., et al. 2018a, *PASJ*, 70, S1
Miyazaki, S., et al. 2018b, *PASJ*, 70, S27
Miyazaki, S., Hamana, T., Ellis, R. S., Kashikawa, N., Massey, R. J., Taylor, J., & Refregier, A. 2007, *ApJ*, 669, 714
Navarro, J. F., Frenk, C. S., & White, S. D. M. 1997, *ApJ*, 490, 493
Oguri, M. 2014, *MNRAS*, 444, 147
Oguri, M., et al. 2018a, *PASJ*, 70, S20
Oguri, M., et al. 2018b, *PASJ*, 70, S26
Oguri, M., & Blandford, R. D. 2009, *MNRAS*, 392, 930
Oguri, M., & Hamana, T. 2011, *MNRAS*, 414, 1851
Planck Collaboration 2016, *A&A*, 594, A27
Pratt, G. W., Arnaud, M., Biviano, A., Eckert, D., Ettori, S., Nagai, D., Okabe, N., & Reiprich, T. H. 2019, *Space Sci. Rev.*, 215, 25
Rykoff, E. S., et al. 2014, *ApJ*, 785, 104
Schirmer, M., Erben, T., Hettterscheidt, M., & Schneider, P. 2007, *A&A*, 462, 875
Schneider, P. 1996, *MNRAS*, 283, 837
Shan, H., et al. 2012, *ApJ*, 748, 56
Shan, H., et al. 2018, *MNRAS*, 474, 1116
Shan, H. Y., et al. 2014, *MNRAS*, 442, 2534
Takahashi, R., Sato, M., Nishimichi, T., Taruya, A., & Oguri, M. 2012, *ApJ*, 761, 152
Tanaka, M., et al. 2018, *PASJ*, 70, S9
Umetsu, K. 2020, *A&AR*, 28, 7
Umetsu, K., & Broadhurst, T. 2008, *ApJ*, 684, 177
Umetsu, K., et al. 2015, *ApJ*, 806, 207
Utsumi, Y., Miyazaki, S., Geller, M. J., Dell'Antonio, I. P., Oguri, M., Kurtz, M. J., Hamana, T., & Fabricant, D. G. 2014, *ApJ*, 786, 93
Voges, W., et al. 1999, *A&A*, 349, 389
Wen, Z. L., & Han, J. L. 2015, *ApJ*, 807, 178
Wen, Z. L., Han, J. L., & Liu, F. S. 2012, *ApJS*, 199, 34
White, M., van Waerbeke, L., & Mackey, J. 2002, *ApJ*, 575, 640
Wittman, D., Dell'Antonio, I. P., Hughes, J. P., Margoniner, V. E., Tyson, J. A., Cohen, J. G., & Norman, D. 2006, *ApJ*, 643, 128
Wittman, D., Tyson, J. A., Margoniner, V. E., Cohen, J. G., & Dell'Antonio, I. P. 2001, *ApJ*, 557, L89
York, D. G., et al. 2000, *AJ*, 120, 1579
Zhang, Y., et al. 2019, *MNRAS*, 487, 2578